Visualization of Carrier Transport in Lateral Metal-Perovskite-Metal Structures and its Influence on Device Operation

N. Ganesh,[1] A.Z. Ashar,[1] Sumukh Purohit,[1] K.L. Narasimhan,[2] and K.S. Narayan[1,3,*]

[1] *Chemistry and Physics of Materials Unit (CPMU), Jawaharlal Nehru Center for Advanced Scientific Research, Jakkur, Bengaluru, 560064, India*

[2] *Center for Nano Science and Engineering (CENSE), Indian Institute of Science, Bengaluru, 560012, India*

[3] *School of Advanced Materials (SAMat), Jawaharlal Nehru Center for Advanced Scientific Research, Jakkur, Bengaluru, 560064, India*

(Received 26 August 2021; revised 3 December 2021; accepted 25 January 2022; published 23 February 2022)

The high performance of hybrid perovskite-based devices is attributed to its excellent bulk transport properties. However, carrier dynamics, especially at the metal-perovskite interface, and their influence on device operation are not widely understood. This work presents the dominant transport mechanisms in methylammonium lead iodide ($MAPbI_3$) perovskite-based asymmetric metal electrode lateral devices. The device operation is studied with interelectrode lengths varying from 4 μm to 120 μm. Device characteristics indicate distinct ohmic and space-charge-limited current regimes that are controlled by the interelectrode length and applied bias. The electric-potential mapping using Kelvin-probe microscopy across the device indicates minimal ion-screening effects and the presence of a transport barrier at the metal-$MAPbI_3$ junction. Furthermore, photocurrent imaging of the channel using near-field excitation-scanning microscopy reveals dominant recombination and charge-separation zones. These lateral devices exhibit photodetector characteristics with a responsivity of about 51 mA/W in self-powered mode and 5.2 A/W at 5 V bias in short-channel devices (4 μm). The low device capacitance enables a fast light-switching response of approximately 12 ns.

DOI: 10.1103/PhysRevApplied.17.024060

I. INTRODUCTION

Hybrid organic-inorganic perovskites (HOIPs) have evolved as attractive materials for optoelectronic applications. These materials have exhibited high performance in solar cells, photodetectors, light-emitting diodes, neuromorphic devices, and lasing applications [1–7]. The excellent performance of these devices is attributed to their outstanding bulk transport properties such as long diffusion length, extended carrier lifetimes, high absorption coefficient, and mobility [8–11]. However, interfacial charge transport dynamics, especially across the metal-perovskite interface, are not widely understood. Despite numerous reports related to devices based on metal-perovskite junctions, the transport dynamics have not been explored in detail [12–14]. Moreover, the study of carrier transport in the space-charge regime is not conclusive. One of the reasons for this discrepancy is that the experimental studies are carried out on sandwich devices, where ionic motion affects carrier transport, even under equilibrium conditions. The present study demonstrates that the lateral structure is a suitable framework to separate the effects of carrier transport and ionic motion. In this work, we study the carrier transport regimes in a HOIP-based lateral metal-semiconductor-metal (*M-S-M*) device as a function of interelectrode distance and applied bias. The lateral geometry provides access to spatially probe the transport parameters such as the local potential and photocurrent across the device. These spatially resolved measurements carried out in tandem with the bulk device characteristics provide a more comprehensive picture of the microscopic origins of carrier transport that affect the device response.

The transport studies are carried out on lateral back-contact *M-S-M* devices, with methylammonium lead iodide, $MAPbI_3$ (MAPI) as the hybrid-perovskite semiconductor. Unlike the widely used sandwich device architecture, lateral devices offer unique advantages such as: (i) reduced light-absorption losses due to the absence of stacked layers, (ii) low dark currents, which allow for small-signal detection, and (iii) low device capacitance, which reduces the *RC* lifetime, thereby enabling device operation for high-speed applications [15]. This work primarily investigates the transport characteristics of lateral asymmetric electrode devices with dissimilar work function metals, i.e., aluminum (Al) and gold (Au). The choice of metal electrode work functions, namely Al

*narayan@jncasr.ac.in

($\varphi_m = 4.1$ eV) and Au ($\varphi_m = 5.2$ eV) in conjunction with MAPI, allows for selective extraction of the photogenerated electron and hole, respectively. In the latter part of the work, we demonstrate the utility of the lateral device for photodetector application. Transient measurements on these devices show a high-speed response component of approximately 12 ns. These devices also exhibit a high linear dynamic range of 118 dB, spanning close to 6 orders of light intensity variation.

II. RESULTS AND DISCUSSION

A. Device operation

The lateral *M-S-M* devices are fabricated using shadow masks, printed using a two-photon-polymerization-based 3D printer (Nanoscribe GmbH), and mask-lift-off techniques developed in the laboratory. After sequential deposition of Au and Al electrodes on the fused silica substrate, MAPI perovskite is deposited (approximately 200 nm) to form the back-contact lateral device, as shown in Fig. 1(a). The absorption and PL spectra of MAPI films shown in Fig. S1(a) in Ref. [16] indicates a band gap of 1.6 eV. Additionally, the sharp XRD peaks (Fig. S1(b) in Ref. [16]) and the morphology (Fig. S1(c) in Ref. [16]) suggest high crystalline order in these films. A detailed explanation of device fabrication is provided in the experimental section of the Supplemental Material [16]. As shown in the device schematic [Fig. 1(a)], l is the interelectrode channel length, d is the thickness of the metal electrode (80–100 nm), and w is the width of the electrode. In this work, we study device characteristics as a function of interelectrode channel lengths (l) in the range of $4 \leq l \leq 120$ μm. In these devices, the electrode width, $w \gg l$, is in the range of 2–4 mm. The cross-section area of these devices is $w \times d$. Fig. S2(a) in Ref. [16] shows the reflection-microscopy image of the asymmetric electrode device, with $l \sim 12$ μm. These devices can be implemented on to a larger area using

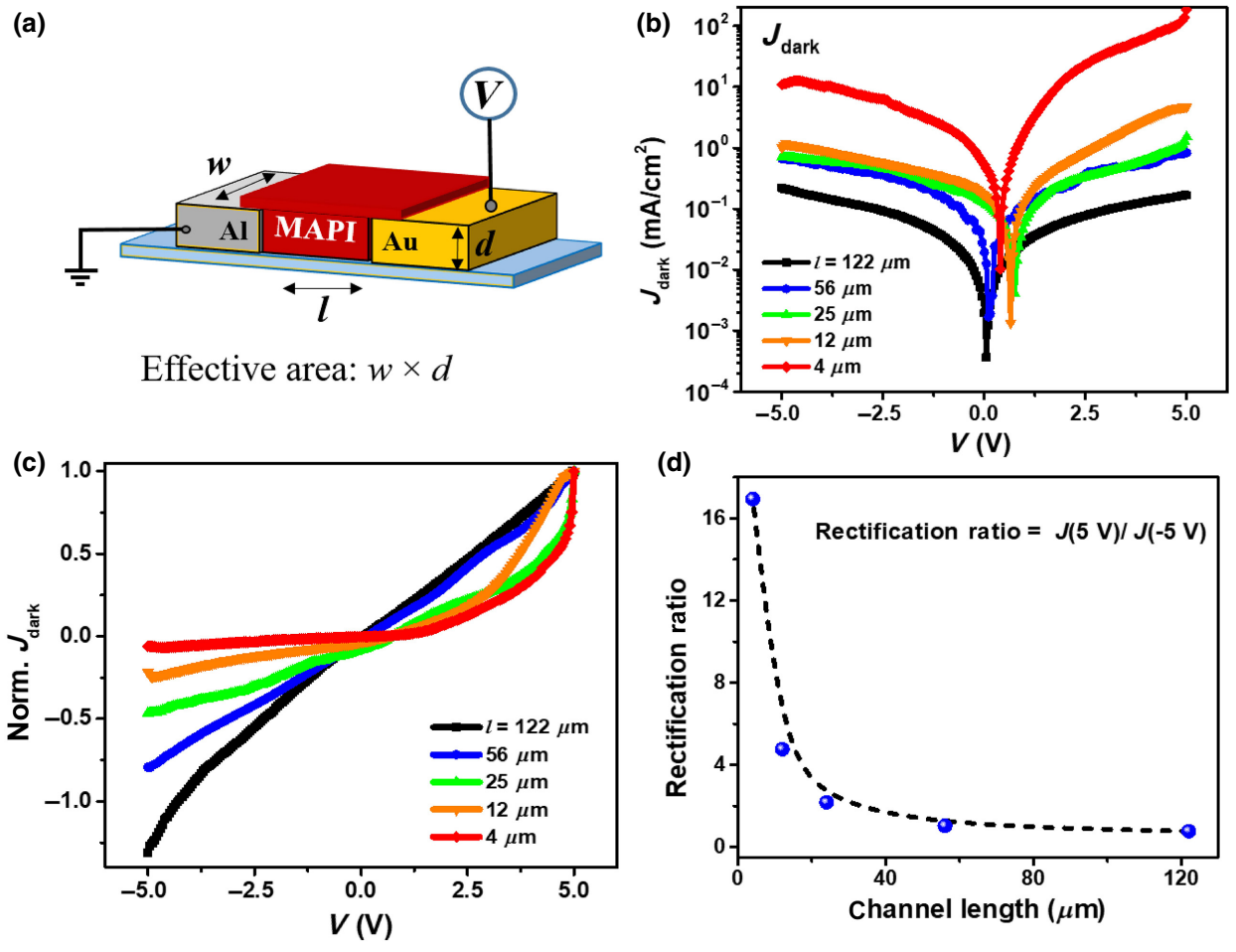

FIG. 1. (a) Schematic of the lateral asymmetric electrode device, where l is the interelectrode channel length and d is the thickness of the metal electrode. (b) Semilog plot of J-V characteristics of the asymmetric electrode device for different values of l. (c) The plot of the J-V characteristics, normalized to J at 5 V bias. (d) The plot of the rectification ratio as a function of channel length shows that the rectification ratio increases for short-channel devices.

interdigitated electrode patterns, as shown in Fig. S2(b) [16].

Figure 1(b) shows the dark current-density–voltage (J-V) characteristics on asymmetric M-S-M devices for different values of the interelectrode distance, l. The magnitude of the dark J at a given voltage increases for the short-channel devices owing to the higher electric field (V/l). Additionally, the J-V features indicate a rectifying behavior in the regime of short-channel devices [Fig. 1(c)]. Likewise, the rectification ratio $= J\ (5\ V)/|J\ (-5\ V)|$, shown in Fig. 1(d) shows a sharp increase for the short-channel devices reaching up to approximately 17 for $l = 4\ \mu$m. To understand the nature of the observed current, we carry out a closer analysis of the nonlinear J-V characteristics.

B. Carrier-transport regimes

Figures 2(a) and 2(b) show the log-log plots of the J-V characteristics for devices with $l = 12$ and 4 μm, respectively, in the positive bias sweep (to the Au electrode). The J-V features are linear (ohmic) at low voltages. Beyond a critical voltage, the current increases as V^2, suggestive of space-charge-limited current (SCLC) behavior and is described by [17,18]

$$J_{\mathrm{SCLC}} = \frac{9}{8}\mu\theta\varepsilon_0\varepsilon_r\frac{V^2}{l^3} \tag{1}$$

where $\mu\theta$, ε_0 and ε_r represent the SCLC mobility, dielectric permittivity and dielectric constant of the semiconductor, respectively. In the expression for the SCLC mobility, $\mu_{\mathrm{SCLC}} = \mu\theta$, μ corresponds to the free carrier mobility, and θ is the reduction factor due to the carrier-trapping effects [19]. The J-V characteristic is linear for longer-channel-length devices ($l > 12\ \mu$m), as depicted in Fig. S3 [16]. However, the transition to the SCLC regime is expected to occur at much larger voltages in agreement with the scaling relation [Eq. (1)].

Figure 2(c) represents the device current as a function of channel length at a bias of 5 V. The current is ohmic ($J \propto l^{-1}$) for long-channel devices ($l > 24\ \mu$m) and scales as l^{-3} for short-channel devices. If the transport is SCLC, J should satisfy a scaling relation such that $J_{\mathrm{SCLC}} = f\ (V^2/l^3)$.

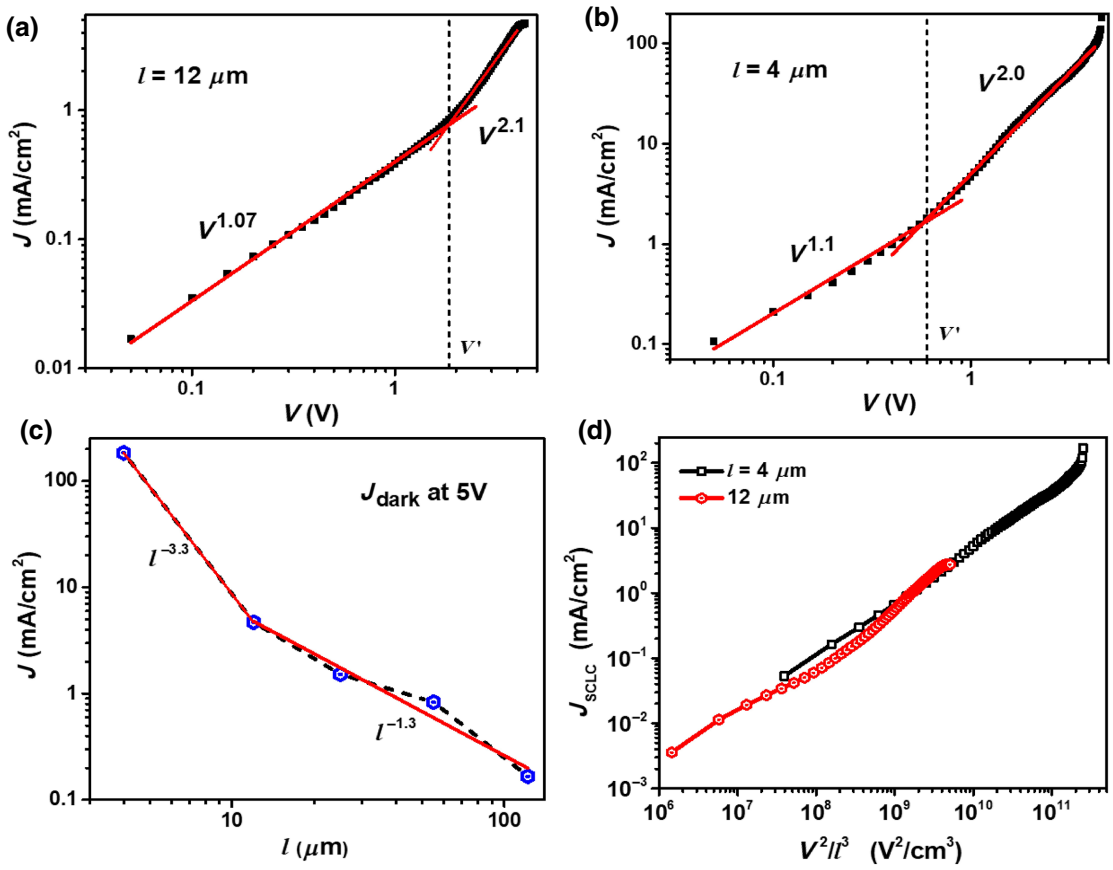

FIG. 2. Log-log plot of the dark J-V data shows distinct ohmic ($\propto V^1$) and SCLC behavior ($\propto V^2$) for (a) $l = 12\ \mu$m and (b) 4 μm channel, respectively. (c) Variation of dark current density at 5 V as a function of channel length shows an ohmic behavior ($\propto l^{-1}$) for the long channel length and an SCLC behavior ($\propto l^{-3}$) for the short channel length. (d) Plot of current density, J_{SCLC} as a function of V^2/l^3 for short-channel devices shows a linear dependence, confirming SCLC behavior.

The SCLC current, J_{SCLC} is estimated considering the device current to be a combination of the ohmic and space-charge limited current, such that $J_{dark} = J_{ohmic} + J_{SCLC}$ [20]. (Details related to the estimation of J_{SCLC} are provided in Sec. 12 of the Supplemental Material [16]). Figure 2(d) is a plot of J_{SCLC} vs V^2/l^3, indicating a linear variation. The current density in the SCLC region is similar for both the $l = 4$ and 12 μm samples. This confirms that the transport in these samples is SCLC. Using Eq. (1) and $\varepsilon_r = 60$ [21,22], the SCLC mobility is determined to be in the range $\mu_{SCLC} \approx 0.07$–0.15 cm^2/Vs. These values are consistent with previous observations of μ from FET and contact-based measurements [19,23–26]. The low lateral mobility in this system is attributed to scattering at the grain boundaries accompanied by carrier-trapping effects. Additionally, the plot in Fig. S4 [16] shows the linear J-V characteristics for positive potential sweep to the Al electrode [negative bias sweep in Fig. 1(b)] for different values of the channel length. It is noted that this rectifying characteristic is not observed in the case of symmetric electrode devices (Fig. S5 in Ref. [16]). Therefore, the origin of this trend is attributed to the presence of a charge-selective transport barrier across either of the metal-perovskite interfaces. To investigate this further, we examine the energy levels and band-bending mechanism across the metal-perovskite interface.

C. Spatial potential mapping

Figure 3(a) shows the band energy levels and the work function of the metal electrodes in the absence of circuit formation. The work function of Al and MAPI are determined to be 4.1 and 5.1 eV, respectively, using Kelvin-probe measurements (with Au as the reference, details in the experimental section, Supplemental Material [16]). The higher work function of MAPI (5.1 eV) attributing a p-type character is consistent with previous observations [27,28], and the hole-carrier concentration is estimated to be approximately 10^{14} cm^{-3}. Upon forming a contact in the short-circuit condition, the Fermi level equilibrates and band bending occurs at the metal-perovskite interface, as shown in Fig. 3(b). At the Al/MAPI interface, this results in an electron injection barrier $\varphi_{bn} = \varphi_m - \chi$ and a hole injection barrier, $\varphi_{bp} = I.E - \varphi_m$, where χ and $I.E$ are the

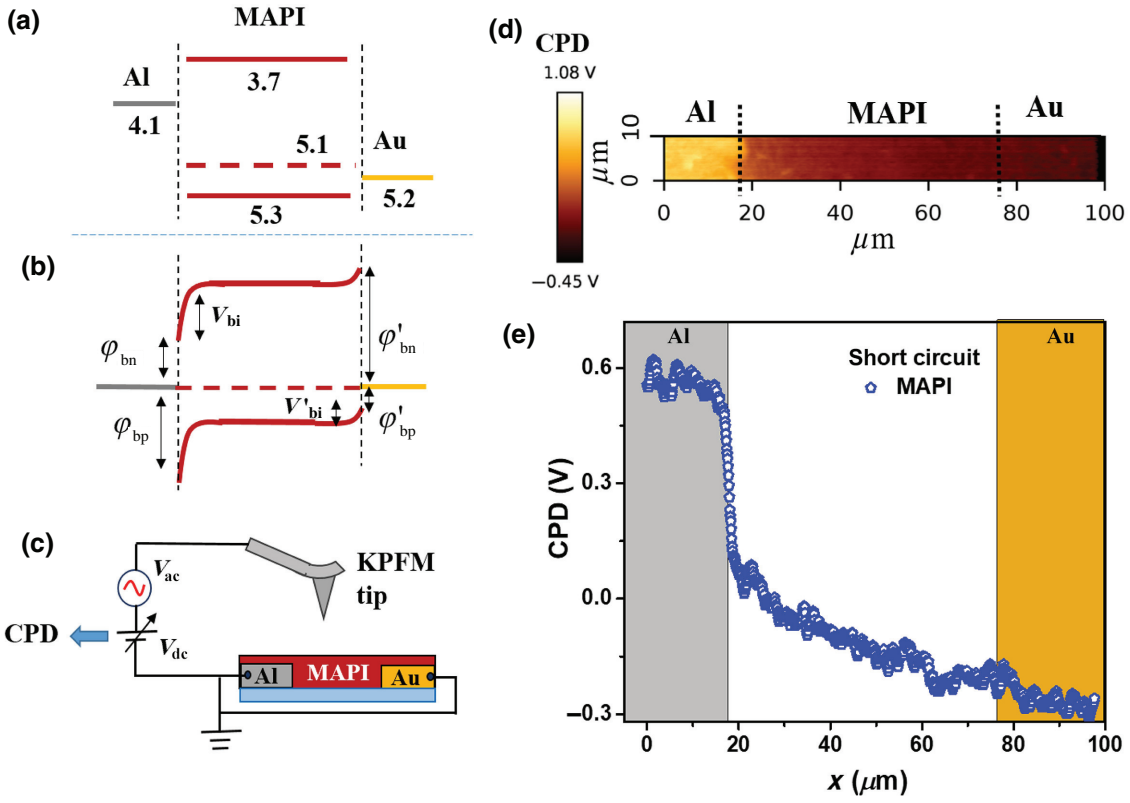

FIG. 3. (a) Band alignment diagram of the asymmetric electrode *M-S-M* device. (b) The device in the short-circuit condition shows an injection barrier at the metal-perovskite interface. A built-in potential, V_{bi} is developed at the metal/MAPI interface as a result of Fermi-level equilibration. (c) Schematic of the KPFM experimental setup used for potential mapping. The measured CPD is used to measure the potential profile across the device. (d) A 2D surface plot of the CPD measured across the device. (e) The CPD linescan profile shows a significant potential drop at the Al/MAPI interface and across the bulk of the device. The potential drop across the Au/MAPI interface is minimal.

electron affinity and ionization energy, respectively. Similar arguments govern the Au/MAPI interface, with an injection barrier for the electrons and holes represented as φ'_{bn} and φ'_{bp}, respectively. A detailed analysis for estimating barrier heights at the Al/MAPI interface and the Au/MAPI interface is elaborated in Fig. S6 [16]. This analysis indicates the presence of a finite injection barrier for both the carriers at the Al/MAPI interface. In contrast, the injection barrier for the holes at Au/HOIP is minimal (approximately 0.1 eV) and can be assumed to be negligible. Additionally, a built-in potential is observed in the perovskite [in Fig. 3(b)], represented as V_{bi} and V'_{bi} at the Al/MAPI and Au/MAPI interface, respectively, that arises as a result of band bending at the interface. In the event of excess carrier generation, this built-in field facilitates electron and hole extraction to the Al and Au electrode, respectively.

The lateral device structure offers the ability to locally probe and map the potential using Kelvin probe force microscopy (KPFM). The KPFM technique, depicted in Fig. 3(c), essentially consists of a conductive tip that is in intermittent contact with the sample. As the tip is scanned across the device, a varying dc potential with an overriding ac bias is applied. At the point of Fermi-level equilibration between the tip and the sample, the contact potential difference (CPD), a parameter proportional to the surface potential, is recorded. Figure 3(d) shows the two-dimensional (2D) surface plot of the CPD across the device (2D surface plots representing morphology and CPD correlation are presented in Fig. S7 in Ref. [16]). In concurrence with the metal work function, the CPD shows a higher value for the Al electrode and a low value for the Au electrode. Figure 3(e) shows the linescan profile of CPD across the device. The difference in the CPD value corresponding to the two electrodes is approximately 0.9 eV, which is in close agreement with the estimated value of 1.1 eV (Fig. S6 in Ref. [16]). As expected, we observe a sharp potential drop across the Al/MAPI interface, which indicates the presence of a high V_{bi} and an injection barrier at the interface. In contrast, at the Au/HOIP interface, the potential drop is minimal, suggesting a pseudo-ohmic contact for the hole carriers. Interestingly, across the bulk of the device, a gradual reduction of the CPD reveals the presence of a built-in electric field, indicative of negligible screening due to the mobile ions at the metal-perovskite interface. Any degrading process resulting from ion accumulation at short-circuit operation is minimal [29]. Moreover, in the presence of low bias and low field conditions, degradation due to ionic drifts is not significant. It is to be noted that in our measurements on back-contact lateral devices, the CPD corresponding to the metal surface is modified due to the presence of a thin layer (approximately 50 nm) of the MAPI perovskite, as depicted in Fig. 3(c). However, the spatial profile is indicative of the potential map across the lateral structure. This is additionally verified by imaging the potential profile in the presence of an external bias.

The previously illustrated transport barrier at the Al/MAPI interface explains the observed rectifying behavior in these asymmetric electrode devices. Essentially, in the negative bias condition (positive voltage to Al), an injection barrier is present for the holes and electrons at the Al/MAPI and Au/MAPI interface, respectively. However, a high forward bias current is observed in the presence of a positive bias, with an efficient injection of holes across the Au/MAPI interface. Therefore, the determined SCLC mobility corresponds to the injected hole carriers. The asymmetry in the J-V (for short-channel devices) shown in Fig. 1(c) then arises from the fact that Al does not make an ohmic contact with MAPI.

Previous reports on HOIP-based devices have shown that the classic SCLC formalism is invalid for systems with mobile ions [29–31]. The effect of ionic conduction is especially amplified in sandwich devices with an active layer thickness in the range of 200–300 nm. This results in a higher electric field (approximately 10^5 V/cm) with the dominant voltage drop across the metal/MAPI interface, thereby completely screening the bulk even in short-circuit conditions [32,33]. On the other hand, in lateral structures, the low electric field (approximately 10^2 V/cm) across the bulk of the lateral device [Fig. 3(e)] suggests the minimal influence of ionic motion.

D. Spatial photocurrent mapping

We study the spatial photocurrent map using a narrowly localized excitation which is scanned across the lateral device. These results are correlated with the KPFM data to gain additional insight regarding photocarrier transport in the background of the imaged potential landscape. The near-field scanning photocurrent microscopy (NSPM) technique is employed to carry out these studies. The experimental setup, as depicted in Fig. 4(a), consists of a tapered optical fiber tip which is integrated with a tuning fork. Using a resonant-frequency-based feedback system, the tuning fork and the fiber tip assembly is lowered to be in close proximity to the device (experimental details provided in the Supplemental Material [16]). With the sample-to-fiber-tip distance in the near-field approximation ($\leq\lambda_{ex}$), beyond Abbe's diffraction limit, spot sizes up to approximately 100 nm can be achieved [34–36].

Figure 4(b) shows the short-circuit photocurrent (I_{ph}) profile as the excitation is scanned across the asymmetric electrode device with $l = 22$ μm. The $I_{ph}(x)$ profile indicates regions of low and high I_{ph} for excitation close to the MAPI/Al and MAPI/Au interface, respectively. The higher I_{ph} close to the Au electrode can be attributed to the efficient transport of the holes to the Au electrode. A model for understanding the reduction of the I_{ph} close to the electrodes needs to be developed. It is to be noted

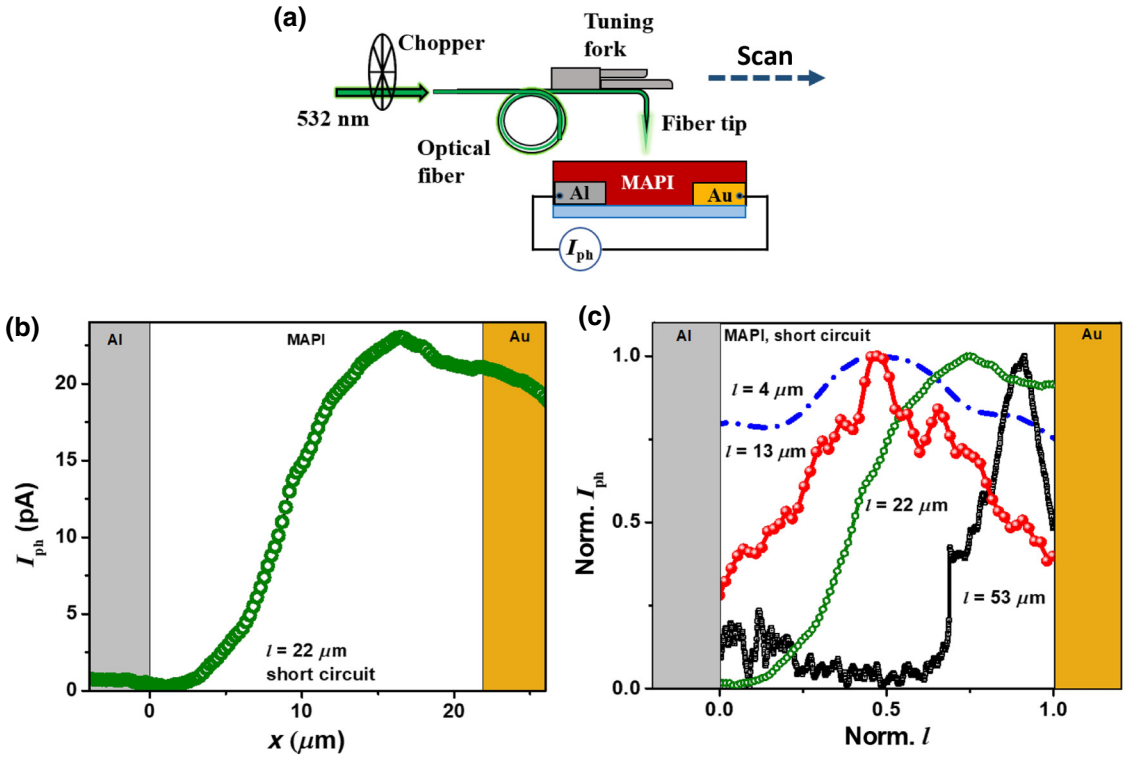

FIG. 4. (a) Schematic of NSPM setup. A tapered fiber tip in near-field excitation is scanned across the lateral device. (b) $I_{ph}(x)$ profile obtained for NSPM scan across $l = 22$ μm *M-S-M* device shows the high I_{ph} for excitation close to the Au/MAPI interface. (c) Normalized $I_{ph}(x)$ profile as a function of channel length. For the short-channel-length devices, $I_{ph}(x)$ tends to a uniform distribution profile.

that for local excitation, the magnitude of the I_{ph} is also controlled by the dark resistance of the channel region outside of the illumination zone. The dark interfacial contact resistance is expected to be relatively higher in the short-channel devices [37]. Possible origins of the low I_{ph} close to the Al interface point to high recombination, presumably due to the presence of interfacial traps or a complex heterojunction.

The influence on the $I_{ph}(x)$ profile is also studied as a function of l, results of which are presented in a normalized plot shown in Fig. 4(c) (raw data in Fig. S8, [16]). For longer $l = 56$ μm, the nonuniformity of the I_{ph} distribution is skewed towards the MAPI/Au interface. However, for a shorter channel $l = 13$ μm, we see that the $I_{ph}(x)$ peak is at the center, and the profile tends to a uniform spatial distribution. The dashed line for $l = 4$ μm, which is the $I_{ph}(x)$ estimated using interpolation, also shows a higher degree of spatial uniformity.

E. Bias-dependence

To understand the microscopic transport features in the entire regime of device operation, we study the potential profiles in the presence of an applied bias. Figure 5(a) shows the KPFM images of the lateral devices, with 5 V applied alternately to the Al and Au electrodes (2D surface plots given in Fig. S9, [16]). In the presence of 5 V applied to the Al electrode, the measured net potential difference across the electrodes is greater than 5 V due to the added contribution of the built-in voltage, i.e., 5 V + V_{bi}. On the other hand, when 5 V is applied to the Au electrode, the net potential difference across the electrodes is less than 5 V or 5 V − V_{bi}. Interestingly, the potential drop across the bulk of the device indicates a gradual reduction, suggesting a constant electric field (Fig. S10 in Ref. [16]). In the case of negative bias (i.e., 5 V to Al), we observe a considerable potential drop across the MAPI/Al interface, indicative of a transport-barrier zone. The reduced dark J in the reverse bias can be attributed to the inability of hole injection across this barrier. Previous works on lateral devices report dominant ion-migration effects under high electric fields over long timescales [38,39]. In our studies, experimental measurements are performed under conditions of low electric field ($<10^4$ V/cm) and shorter timescales to minimize the influence of ionic motion.

In the presence of an applied bias, the band-bending directionality allows for photocarrier extraction to the respective electrodes. This photocarrier extraction efficiency also depends on the carrier mobility and position of excitation from the collection electrode. Figure 5(b) shows

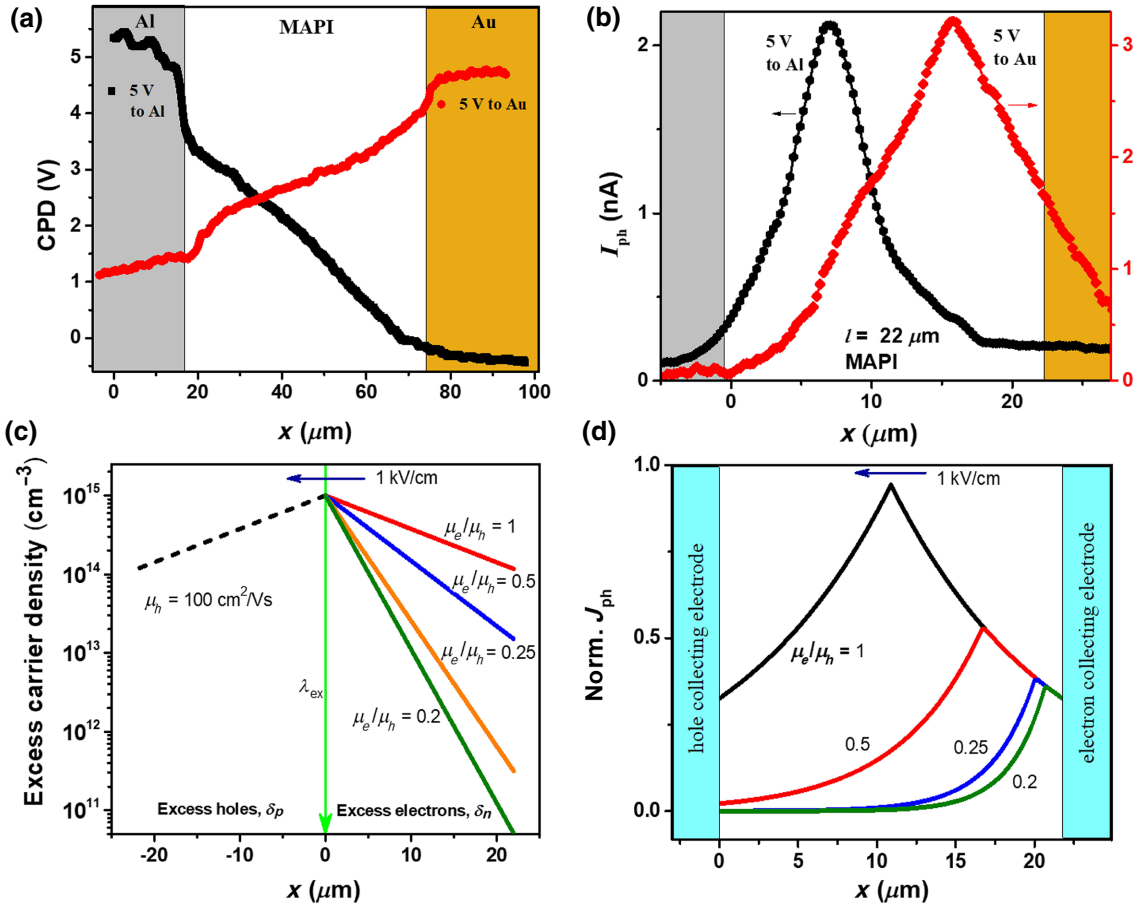

FIG. 5. (a) CPD profiles from KPFM on *M-S-M* devices for positive and negative bias of 5 V. Alternately, this indicates 5 V applied to either Au or Al electrodes. The gradual potential drop indicates a uniform electric field across the device. (b) NSPM scans in the presence of external bias show the presence of a photocurrent peak that shifts depending on the polarity of the bias. This $I_{\mathrm{ph}}(x)$ asymmetry indicates unbalanced carrier mobility. (c) Simulation using the finite element method shows the decay of excess electrons and holes for excitation at $x = 0$, under conditions of 1D drift-diffusion transport for different μ_e values. (d) The normalized J_{ph} profiles, simulated as a function of excitation position across the device, under 1 kV/cm electric field. The profiles indicate a shift in the $J_{\mathrm{ph}}(x)$ peak in the case of unbalanced carrier mobility, which explains the feature observed in (b).

the $I_{\mathrm{ph}}(x)$ profile obtained from the NSPM technique on the lateral devices in the presence of both a positive and negative bias of 5 V. The profile indicates a spatial asymmetry, where the I_{ph} peak shifts towards the positively biased (the electron extracting) electrode. This polarity-dependent $I_{\mathrm{ph}}(x)$ asymmetry can be attributed to the unbalanced carrier mobility of the hole and the electron. To understand the microscopic picture of these bias-dependent photocurrent profiles, we simulate the carrier and photocurrent profiles using a simplistic one-dimensional (1D) drift-diffusion formalism (details of simulation in Sec. 13 of Supplemental Material [16]). These results emphasize the dominant role of unbalanced mobility and can be obtained from solving the transport equation under conditions of steady-state generation at $x = 0$, a drift condition assuming uniform electric field ($E = 1$ kV/cm), and hole mobility, $\mu_h = 100$ cm^2/Vs (this represents free carrier mobility in the ohmic regime of operation) [11]. Figure 5(c) shows the simulated spatial distribution of the excess photogenerated electrons and holes. The spatial dependence of excess photogenerated carriers can be expressed as

$$\delta n(x) = \delta n_0 \exp\left[-\left(\frac{\sqrt{\left(\mu^2E^2 + \frac{4D}{\tau}\right)} - \mu E}{2D}\right)x\right] \quad (2)$$

where, δn_0, E, D, and τ represent the excess carrier density at the point of generation, electric field, diffusion coefficient, and recombination lifetime, respectively. To account for unbalanced transport, we simulate carrier density profiles for different values of electron mobility, μ_e, which is designated to be a fraction of the hole mobility. Figure 5(c) shows that the electron distribution profiles exhibit a longer decay length for higher μ_e. Additionally, the directionality of hole and electron decay profiles show that holes

drift in the direction of the electric field, and the electrons drift and decay in the opposite direction. Further, to verify the profiles observed in the bias-dependent NSPM experiment [Fig. 5(b)], we simulate the spatial photocurrent density profile, $J_{\rm ph}(x)$, which is given as a combination of diffusion and drift currents

$$J_{\rm ph}(x) = J_{\rm drift} + J_{\rm diffusion} = \delta ne\mu E + eD\frac{\partial\,\delta n}{\partial x} \qquad (3)$$

It is additionally noted that the observed current is a result of net *e-h* recombination in the external circuit. Figure 5(d) presents the simulated normalized photocurrent density profiles for various μ_e/μ_h ratios. The profiles indicate that, in the case of balanced mobility, i.e., $\mu_e = \mu_h$, $I_{\rm ph}$ peaks with excitation at the device center. This region of maxima denotes a zone for the optimal collection of electrons and holes at the respective electrodes. On the other hand, for unbalanced mobility ($\mu_e < \mu_h$), the peak shifts towards the electron-collection electrode. It is additionally noted that the carrier lifetime also affects the distribution profile [as indicated in Eq. (2)]. Overall, the asymmetry of the $I_{\rm ph}(x)$ points to the lower $\mu\tau$ product of the electrons ($\mu_e\tau_e < \mu_h\tau_h$). This interpretation is in agreement with earlier reports [11,40].

F. Photodetector characteristics

The light-dependent J-V characteristics on lateral *M-S-M* devices are shown in Fig. 6(a) under a 532-nm-illumination condition (26 mW/cm^2). The $I_{\rm ph}$ increases for the short-channel devices owing to a higher electric field at any given voltage. It can also be seen that a short-circuit $I_{\rm ph}$ is also observed corresponding to the values at $V = 0$. The directionality of the $I_{\rm ph}$ confirms the electron extraction to the Al electrode and holes to the Au electrode. Figure 6(b) shows the variation of the device responsivity with respect to the channel length. We achieve a responsivity, $R \approx 51$ mA/W in the self-powered mode and $R \approx 5.2$ A/W

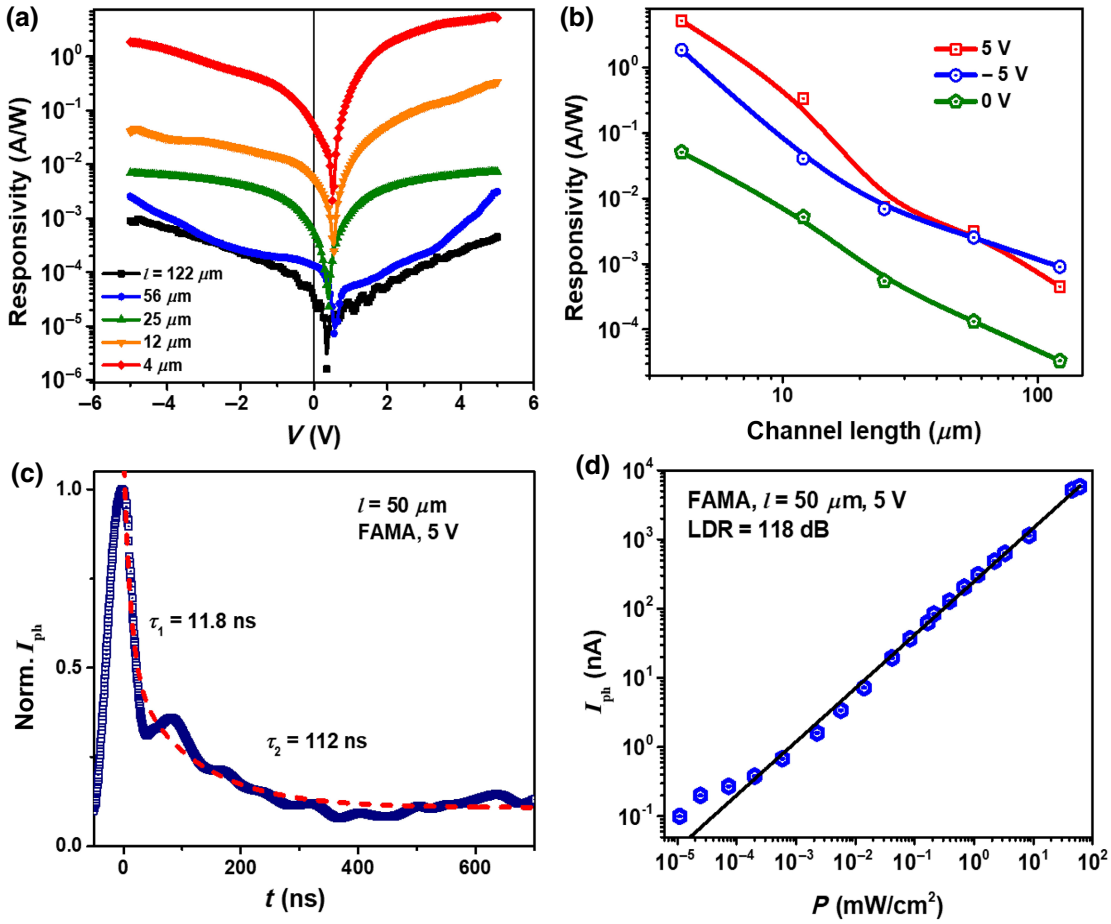

FIG. 6. (a) Voltage-dependent responsivity characteristics of the lateral devices for 532-nm illumination at 26 mW/cm^2. A short-circuit $I_{\rm ph}$ is observed at 0 V. (b) Variation of the responsivity as a function of channel length under short-circuit conditions and ±5 V bias conditions. (c) Transient photocurrent measurement on lateral *M-S-M* devices with mixed-phase perovskite (FAMA) as the active layer. The biexponential fit reveals a fast response time of 11.8 ns followed by a slow component of approximately 112 ns. (d) Variation of photocurrent with respect to light intensity ($\lambda = 532$ nm), shows the LDR ~ 118 dB, spanning over 6 orders of intensity variation.

at 5 V operating voltage for the $l = 4$ μm device. This corresponds to quantum efficiency, QE $= n_{\text{carriers}}/n_{\text{photons}} = 1240R/\lambda$ (Wnm/A) of 11.9% and 1212% at 0 and 5 V, respectively. The gain ($I_{\text{ph}}/I_{\text{dark}}$) observed in these devices is about 10^2 (Fig. S11 in Ref. [16]). The performance of these devices compares with lateral photodetectors reported in the literature [13,41,42].

The lateral devices are characterized by low device capacitance owing to the tiny overlap area across the two metal electrodes. This results in a small *RC* value, which reduces the overall response time of the device [43]. $I_{\text{ph}}(t)$ decay measurements on HOIP-based *M-S-M* devices have reported operational speeds in the range of 40–90 ns [44]. We additionally observe a fast decay component of 11.8 ns [shown in Fig. 6(c)], using transient photocurrent measurements on *M-S-M* devices with mixed-phase perovskite, $FA_{0.82}MA_{0.18}Pb(I_{0.82}Br_{0.18})_3$ (abbreviated as FAMA, where FA = formamidium) as the active semiconductor. Such fast response times allow for applications involving high-speed detectors.

The lateral device structure is characterized by a low dark current in comparison to the sandwich architecture. This reduces the noise level of device operation and allows for weak signal detection, increasing the dynamic range in these devices. Figure 6(d) shows the linear dynamic range (LDR) of the lateral device with the mixed-phase perovskite in the active layer. The device maintains a linear response over a range spanning 6 orders of intensity variation, resulting in a LDR $= 20\log(P_{\text{max}}/P_{\text{min}})$ of 118 dB, where P_{max} and P_{min} correspond to the maximum and minimum light power, respectively, which is resolved with maintained responsivity.

III. CONCLUSION

The lateral asymmetric electrode *M-S-M* devices exhibit distinct transport regimes as a function of applied bias and interelectrode distance. The transport shows ohmic behavior at low voltages and becomes space-charge limited at high voltage in the short-channel-length devices, consistent with the SCLC scaling relation. The observed rectifying *J-V* characteristic is attributed to bias-direction-dependent SCLC behavior due to efficient hole injection across the Au/MAPI interface. The KPFM plots across the device indicate an electric field in bulk, both in short-circuit and bias conditions, suggesting negligible ion-screening effects. In the presence of an applied bias, the spatial photocurrent profiles are understood in the context of drift-diffusion formalism, which indicates unbalanced carrier transport. The lateral devices exhibit photodetection capability and demonstrate a high responsivity of approximately 5.2 A/W at 5 V operating bias in the short-channel structures. In addition to a higher dynamic range spanning 6 orders of intensity variation, the low device capacitance allows for high-speed applications in the gigahertz regime.

ACKNOWLEDGMENTS

The authors acknowledge the Department of Science and Technology, Government of India, and EPSRC-UKRI Global Challenge Research Fund project, SUNRISE (Grant No. EP/P032591/1), for the financial assistance. S.P. acknowledges the DST-INSPIRE program.

[1] Q. Jiang, Y. Zhao, X. Zhang, X. Yang, Y. Chen, Z. Chu, Q. Ye, X. Li, Z. Yin, and J. You, Surface passivation of perovskite film for efficient solar cells, Nat. Photonics **13**, 460 (2019).

[2] N. R. E. Laboratory, Best research-cell efficiency chart (NREL Golden, CO, accessed June 2021).

[3] Y.-H. Lin, N. Sakai, P. Da, J. Wu, H. C. Sansom, A. J. Ramadan, S. Mahesh, J. Liu, R. D. Oliver, and J. Lim, A piperidinium salt stabilizes efficient metal-halide perovskite solar cells, Science **369**, 96 (2020).

[4] Y. Wang, Z. Lv, J. Chen, Z. Wang, Y. Zhou, L. Zhou, X. Chen, and S. T. Han, Photonic synapses based on inorganic perovskite quantum dots for neuromorphic computing, Adv. Mater. **30**, 1802883 (2018).

[5] Y. Wang, R. Fullon, M. Acerce, C. E. Petoukhoff, J. Yang, C. Chen, S. Du, S. K. Lai, S. P. Lau, and D. Voiry, Solution-processed MoS_2/organolead trihalide perovskite photodetectors, Adv. Mater. **29**, 1603995 (2017).

[6] C. Qin, A. S. Sandanayaka, C. Zhao, T. Matsushima, D. Zhang, T. Fujihara, and C. Adachi, Stable room-temperature continuous-wave lasing in quasi-2D perovskite films, Nature **585**, 53 (2020).

[7] L. Zhao, K. Roh, S. Kacmoli, K. Al Kurdi, S. Jhulki, S. Barlow, S. R. Marder, C. Gmachl, and B. P. Rand, Thermal management enables bright and stable perovskite light-emitting diodes, Adv. Mater. **32**, 2000752 (2020).

[8] Z. Chen, Q. Dong, Y. Liu, C. Bao, Y. Fang, Y. Lin, S. Tang, Q. Wang, X. Xiao, and Y. Bai, Thin single crystal perovskite solar cells to harvest below-bandgap light absorption, Nat. Commun. **8**, 1 (2017).

[9] Y. Chen, H. Yi, X. Wu, R. Haroldson, Y. Gartstein, Y. Rodionov, K. Tikhonov, A. Zakhidov, X.-Y. Zhu, and V. Podzorov, Extended carrier lifetimes and diffusion in hybrid perovskites revealed by Hall effect and photoconductivity measurements, Nat. Commun. **7**, 1 (2016).

[10] S. D. Stranks, G. E. Eperon, G. Grancini, C. Menelaou, M. J. Alcocer, T. Leijtens, L. M. Herz, A. Petrozza, and H. J. Snaith, Electron-hole diffusion lengths exceeding 1 micrometer in an organometal trihalide perovskite absorber, Science **342**, 341 (2013).

[11] Q. Dong, Y. Fang, Y. Shao, P. Mulligan, J. Qiu, L. Cao, and J. Huang, Electron-hole diffusion lengths >175 μm in solution-grown $CH_3NH_3PbI_3$ single crystals, Science **347**, 967 (2015).

[12] S. J. Yang, M. Kim, H. Ko, D. H. Sin, J. H. Sung, J. Mun, J. Rho, M. H. Jo, and K. Cho, Visualization and investigation of charge transport in mixed-halide perovskite via lateral-structured photovoltaic devices, Adv. Funct. Mater. **28**, 1804067 (2018).

[13] J. Ding, S. Du, Y. Zhao, X. Zhang, Z. Zuo, H. Cui, X. Zhan, Y. Gu, and H. Sun, High-quality inorganic–organic perovskite $CH_3NH_3PbI_3$ single crystals for photo-detector applications, J. Mater. Sci. **52**, 276 (2017).

[14] X. Lin, A. N. Jumabekov, N. N. Lal, A. R. Pascoe, D. E. Gómez, N. W. Duffy, A. S. Chesman, K. Sears, M. Fournier, and Y. Zhang, Dipole-field-assisted charge extraction in metal-perovskite-metal back-contact solar cells, Nat. Commun. **8**, 1 (2017).

[15] D. G. Georgiadou, J. Semple, A. A. Sagade, H. Forstén, P. Rantakari, Y.-H. Lin, F. Alkhalil, A. Seitkhan, K. Loganathan, and H. Faber, 100 GHz zinc oxide Schottky diodes processed from solution on a wafer scale, Nat. Electron. **3**, 718 (2020).

[16] See Supplemental Material at http://link.aps.org/supplemental/10.1103/PhysRevApplied.17.024060 for thin film characterization data, microscopy images of the lateral devices, log-log plots of the dark *J-V* data, *J-V* characteristics of symmetric devices, 2D surface plots of KPFM data, modeling and simulation details of carrier transport, and experimental section.

[17] N. Mott, *GURNEY RW-Electronic Processes in Ionic Crystals* (Oxford University Press, New York, 1940).

[18] M. A. Lampert and P. Mark, *Current Injection in Solids* (Academic Press New York, London, 1970).

[19] M. S. Alvar, P. W. Blom, and G.-J. A. Wetzelaer, Space-charge-limited electron and hole currents in hybrid organic-inorganic perovskites, Nat. Commun. **11**, 1 (2020).

[20] J. A. Röhr and R. C. MacKenzie, Analytical description of mixed ohmic and space-charge-limited conduction in single-carrier devices, J. Appl. Phys. **128**, 165701 (2020).

[21] M. Zhang, X. Zhang, L.-Y. Huang, H.-Q. Lin, and G. Lu, Charge transport in hybrid halide perovskites, Phys. Rev. B **96**, 195203 (2017).

[22] N. Onoda-Yamamuro, T. Matsuo, and H. Suga, Dielectric study of $CH_3NH_3PbX_3$ (X = Cl, Br, I), J. Phys. Chem. Solids **53**, 935 (1992).

[23] M. Petrovic, T. Ye, V. Chellappan, and S. Ramakrishna, Effect of low temperature on charge transport in operational planar and mesoporous perovskite solar cells, ACS Appl. Mater. Interfaces **9**, 42769 (2017).

[24] D. Li, G. Wang, H.-C. Cheng, C.-Y. Chen, H. Wu, Y. Liu, Y. Huang, and X. Duan, Size-dependent phase transition in methylammonium lead iodide perovskite microplate crystals, Nat. Commun. **7**, 1 (2016).

[25] X. Y. Chin, D. Cortecchia, J. Yin, A. Bruno, and C. Soci, Lead iodide perovskite light-emitting field-effect transistor, Nat. Commun. **6**, 1 (2015).

[26] S. P. Senanayak, B. Yang, T. H. Thomas, N. Giesbrecht, W. Huang, E. Gann, B. Nair, K. Goedel, S. Guha, and X. Moya, Understanding charge transport in lead iodide perovskite thin-film field-effect transistors, Sci. Adv. **3**, e1601935 (2017).

[27] J. R. Harwell, T. Baikie, I. Baikie, J. L. Payne, C. Ni, J. T. S. Irvine, G. A. Turnbull, and I. D. W. Samuel, Probing the energy levels of perovskite solar cells via kelvin probe and UV ambient pressure photoemission spectroscopy, Phys. Chem. Chem. Phys. **18**, 19738 (2016).

[28] Y. Zhou and G. Long, Low density of conduction and valence band states contribute to the high open-circuit voltage in perovskite solar cells, J. Phys. Chem. C **121**, 1455 (2017).

[29] E. A. Duijnstee, J. M. Ball, V. M. Le Corre, L. J. A. Koster, H. J. Snaith, and J. Lim, Toward understanding space-charge limited current measurements on metal halide perovskites, ACS Energy Lett. **5**, 376 (2020).

[30] H. J. Snaith, A. Abate, J. M. Ball, G. E. Eperon, T. Leijtens, N. K. Noel, S. D. Stranks, J. T.-W. Wang, K. Wojciechowski, and W. Zhang, Anomalous hysteresis in perovskite solar cells, J. Phys. Chem. Lett. **5**, 1511 (2014).

[31] W. Tress, Metal halide perovskites as mixed electronic–ionic conductors: Challenges and opportunities-from hysteresis to memristivity, J. Phys. Chem. Lett. **8**, 3106 (2017).

[32] S. A. Weber, I. M. Hermes, S.-H. Turren-Cruz, C. Gort, V. W. Bergmann, L. Gilson, A. Hagfeldt, M. Graetzel, W. Tress, and R. Berger, How the formation of interfacial charge causes hysteresis in perovskite solar cells, Energy Environ. Sci. **11**, 2404 (2018).

[33] H. Wang, A. Guerrero, A. Bou, A. M. Al-Mayouf, and J. Bisquert, Kinetic and material properties of interfaces governing slow response and long timescale phenomena in perovskite solar cells, Energy Environ. Sci. **12**, 2054 (2019).

[34] C. R. McNeill, H. Frohne, J. L. Holdsworth, J. E. Furst, B. V. King, and P. C. Dastoor, Direct photocurrent mapping of organic solar cells using a near-field scanning optical microscope, Nano Lett. **4**, 219 (2004).

[35] S. Mukhopadhyay, A. J. Das, and K. Narayan, High-resolution photocurrent imaging of bulk heterojunction solar cells, J. Phys. Chem. Lett. **4**, 161 (2013).

[36] S. Mukhopadhyay, S. Ramachandra, and K. Narayan, Direct observation of charge generating regions and transport pathways in bulk heterojunction solar cells with asymmetric electrodes using near field photocurrent microscopy, J. Phys. Chem. C **115**, 17184 (2011).

[37] M. Rao and K. Narayan, Evaluation of electrode-semiconductor barrier in transparent top-contact polymer field effect transistors, Appl. Phys. Lett. **92**, 201 (2008).

[38] F. Liu, L. Wang, J. Wang, F. Wang, Y. Chen, S. Zhang, H. Sun, J. Liu, G. Wang, and Y. Hu, 2D ruddlesden–popper perovskite single crystal field-effect transistors, Adv. Funct. Mater. **31**, 2005662 (2021).

[39] Y. Yuan, J. Chae, Y. Shao, Q. Wang, Z. Xiao, A. Centrone, and J. Huang, Photovoltaic switching mechanism in lateral structure hybrid perovskite solar cells, Adv. Energy Mater. **5**, 1500615 (2015).

[40] O. E. Semonin, G. A. Elbaz, D. B. Straus, T. D. Hull, D. W. Paley, A. M. Van der Zande, J. C. Hone, I. Kymissis, C. R. Kagan, and X. Roy, Limits of carrier diffusion in n-type and p-type $CH_3NH_3PbI_3$ perovskite single crystals, J. Phys. Chem. Lett. **7**, 3510 (2016).

[41] Y. Liu, Y. Zhang, K. Zhao, Z. Yang, J. Feng, X. Zhang, K. Wang, L. Meng, H. Ye, and M. Liu, A 1300 mm^2 ultrahigh-performance digital imaging assembly using high-quality perovskite single crystals, Adv. Mater. **30**, 1707314 (2018).

[42] B. Yang, F. Zhang, J. Chen, S. Yang, X. Xia, T. Pullerits, W. Deng, and K. Han, Ultrasensitive and fast all-inorganic

perovskite-based photodetector via fast carrier diffusion, Adv. Mater. **29**, 1703758 (2017).

[43] A. Armin, M. Hambsch, I. K. Kim, P. L. Burn, P. Meredith, and E. B. Namdas, Thick junction broadband organic photodiodes, Laser & Photonics Reviews **8**, 924 (2014).

[44] F. X. Liang, J. Z. Wang, Z. X. Zhang, Y. Y. Wang, Y. Gao, and L. B. Luo, Broadband, ultrafast, self-driven photodetector based on Cs-doped $FAPbI_3$ perovskite thin film, Adv. Opt. Mater. **5**, 1700654 (2017).